Epi-illumination diffraction phase microscopy with white light

C. Edwards,[1,2] B. Bhaduri,[2] B. G. Griffin,[1] L. L. Goddard,[1] and G. Popescu[2,*]

[1]*Photonic Systems Laboratory, Department of Electrical and Computer Engineering, Micro and Nanotechnology Laboratory, University of Illinois at Urbana-Champaign, Urbana, Illinois 61801, USA*

[2]*Quantitative Light Imaging Laboratory, Department of Electrical and Computer Engineering, Beckman Institute for Advanced Science and Technology, University of Illinois at Urbana-Champaign, Urbana, Illinois 61801, USA*

Corresponding author: gpopescu@illinois.edu

We demonstrate the first reflection-based epi-illumination diffraction phase microscope with white light (epi-wDPM). The epi-wDPM system combines the off-axis, common-path, and white light approaches, in a reflection geometry enabling sub-nanometer spatial and temporal noise levels, while providing single-shot acquisition for opaque samples. We verified the epi-wDPM results by measuring control samples with known dimensions and comparing them to measurements from other well-established techniques. We imaged gold-coated HeLa cells to illustrate the tradeoffs between epi-wDPM with low and high spatial coherence.   © 2014 Optical Society of America

OCIS codes: (170.0110) Imaging systems; (120.3180) Interferometry; (120.4630) Optical inspection; (120.5050) Phase measurement; (160.0160) Materials.

http://dx.doi.org/10.1364/OL.39.006162

The development of lasers and personal computers enabled great leaps in precision optical metrology and material characterization [1,2]. Today, a wide variety of techniques are commonly used including scanning electron microscopy (SEM) [3], atomic force microscopy (AFM) [4], scanning white-light interferometry [5], phase-shifting interferometry [6], and digital holography [7].

Quantitative phase imaging, or QPI, techniques utilize not only the *amplitude* of the imaging field, but also its *phase* in order to provide quantitative topographical and/or refractive index data [8,9]. As light from the source interacts with the sample, a *fingerprint* of the structure is encoded into the phase front of the imaging field, which can then be used to reconstruct a map of the sample's surface. Visible light contains frequencies of several hundred terahertz, which is far too fast for electronic detectors to measure the field directly; instead, they obtain only the intensity. For this reason, various QPI techniques have been developed to help gain access to this valuable phase information [8].

Diffraction phase microscopy (DPM) combines many of the best attributes of current QPI techniques [10,11]. Its compact, off-axis approach takes advantage of both the low spatiotemporal noise and fast acquisition rates of previous QPI techniques [10,12,13]. DPM using laser illumination has been demonstrated in both transmission and reflection modes, to accommodate both transparent and opaque samples, and has been used in a wide variety of biological and materials science applications [11].

Recently, DPM using white-light illumination (wDPM) was developed in transmission mode for use in biological studies [14]. QPI systems using white-light illumination, require more precise alignment, but exhibit lower noise levels than their laser counterparts [11,14–16]. This is a result of the lower coherence, both temporally and spatially, which reduces speckle [17]. When used with insufficient spatial filtering, white-light systems exhibit object-dependent artifacts, such as the well-known *halo effect* [18,19], which disrupt the accuracy of quantitative

measurements [14,20,21]. Such effects are typically mild for small weakly scattering transparent structures like cells and neurons, but are much more prominent when imaging large opaque structures in reflection. This makes implementing wDPM in reflection for use in materials science applications challenging. Recently, we have shown that such artifacts are a high-pass filtering phenomenon caused by lack of spatial coherence [21]. This realization allowed us to quantitatively model the phase reductions and halo effect [22] and remove them experimentally through system redesign [21].

Here, we present a combined DPM/wDPM system capable of providing halo-free images of structures typical in both materials science and biological applications. The microscope operates in both transmission and reflection modes in order to accommodate both transparent and opaque samples. The DPM/wDPM system is implemented as an add-on module that can be placed at the output port of any conventional light microscope. Figure 1 shows a schematic of the combined system which has four components: (1) DPM (laser transmission), (2) epi-DPM (laser reflection), (3) wDPM (white-light transmission), and (4) epi-wDPM (white-light reflection). The first three components have been previously demonstrated and, thus, are drawn in faded color. The user can switch between laser and white-light sources as well as transmission and reflection simply by flipping switches on the microscope. Also, the spatial coherence for wDPM can be optimized for the given application by rotating the condenser turret in transmission, or adjusting the slider for the aperture diaphragm in reflection, which contain different size pinholes, allowing for a trade-off between accuracy and speed.

To gain access to the phase of the imaging field, DPM uses a diffraction grating, a $4f$ lens system, and a pinhole filter to create a compact Mach–Zehnder interferometer. The two fields interfere at the CCD and produce a spatially modulated signal, which allows us to extract the phase information via a Hilbert transform [11,15,23].
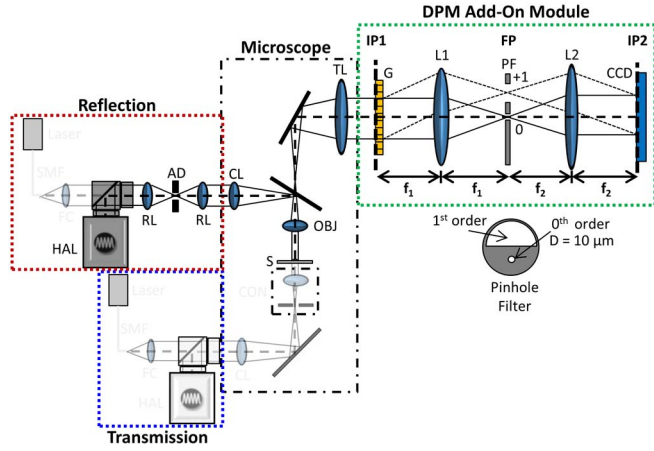
Fig. 1. Combined DPM/wDPM setup. Abbreviations: SMF, single mode fiber; FC, fiber collimator; HAL, halogen lamp; RL, relay lens; AD, aperture diaphragm; CL, collector lens; CON, condenser; OBJ, objective; S, sample; TL, tube lens; L1/L2, lenses.

Note that all lenses in the setup are achromatic to minimize chromatic aberrations when using white light.

For reflection-based DPM, assuming adequate spatial coherence and proper filtering of the reference beam [15], the interferogram measured at the CCD is:

$$I(x,y) = I_0 + I_1(x,y) \\ + 2\sqrt{I_0 I_1(x,y)} \cos[\beta x + \Delta\phi(x,y)], \quad (1)$$

where I_0 and I_1 are the irradiance of the reference and imaging fields, respectively. The modulation frequency at the sample plane is $\beta = 2\pi M_{obj}/\Lambda$, where Λ is the period of the grating and M_{obj} is the magnification of the microscope with the current objective. The extracted phase is:

$$\Delta\phi(x,y) = \phi_1(x,y) - \phi_0, \quad (2)$$

where ϕ_1 is the desired phase image and ϕ_0 is a constant that is subtracted out by setting the background of the image to zero. If necessary, the Goldstein algorithm, which is a good compromise between computation time and accuracy, can be employed to unwrap the phase [11]. The height map is then obtained as follows:

$$h(x,y) = \frac{\bar{\lambda}_0}{4\pi n} \phi_1(x,y), \quad (3)$$

where h is the height and $\bar{\lambda}_0$ is the mean wavelength of the source. Note the additional factor of 2 due to the double pass in reflection and that the refractive index n is for the surrounding medium, which is typically air.

In order to validate the measurements taken under the new reflection-based white-light DPM (epi-wDPM) configuration, control samples were fabricated with known dimensions. The samples consisted of reflective nanopillars (patterned quartz coated with gold) of various widths as well as the 1951 USAF resolution target. The heights of all structures were validated by the Alpha Step IQ Profilometer. All images in this article were taken using a 20×, 0.8 NA objective, resulting in a field of view of $140\,\mu m \times 180\,\mu m$. Figures 2(a) and 2(b) show the
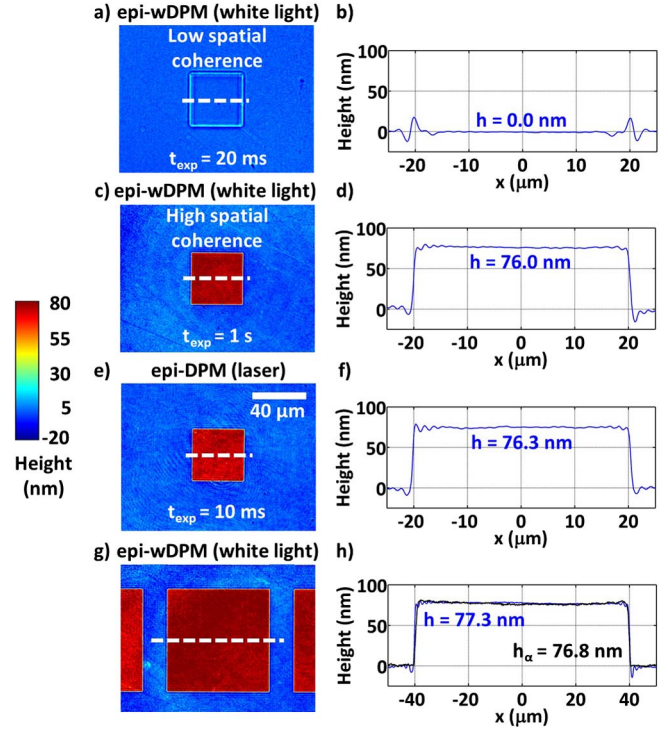

Fig. 2. Epi-wDPM validation. (a), (b) epi-wDPM (white light) height map and corresponding cross-section taken from dotted line in (a) of a 40-μm width nanopillar. Insufficient spatial coherence results in incorrect height measurements. (c), (d) epi-wDPM (white light) height map and corresponding cross-section. Sufficient spatial coherence reveals proper topography at the expense of longer exposure times. (e), (f) epi-DPM (laser) height map and corresponding cross-section. (g), (h) epi-wDPM (white light) height map and corresponding cross-section of a 80-μm width nanopillar, which requires more spatial coherence. The Alpha Step validation is shown in (h).

epi-wDPM height map and corresponding cross-section for a 40-μm width nanopillar imaged with the aperture diaphragm fully closed. Simply closing the aperture diaphragm does not provide the necessary spatial coherence to get proper topographical data. To correct this, the spatial coherence was selected using a small enough pinhole (10 μm) in the aperture diaphragm such that the mutual intensity function is nearly uniform over the field of view (FOV). This allows the system to properly image any structure that fits within the FOV [21]. Figures 2(c), 2(d) show that accurate height maps are obtained using white light once the spatial coherence is sufficient. Figures 2(e), 2(f) show the height map and cross-section using laser illumination (epi-DPM). This technique has already been demonstrated [15], and the results are used here as a benchmark. Figures 2(g), 2(h) show the epi-wDPM height map and corresponding cross-section of an 80-μm pillar, which barely fits in the FOV and requires greater spatial coherence for quantitatively accurate, halo-free height maps. The Alpha Step profile is also shown in Fig. 2(h) for further validation. The exposure times, t_{exp}, used for each configuration are displayed in the subfigures for comparison. White-light with high spatial coherence requires longer exposure times due to spatial filtering. This can be circumvented by using a supercontinuum laser [21].
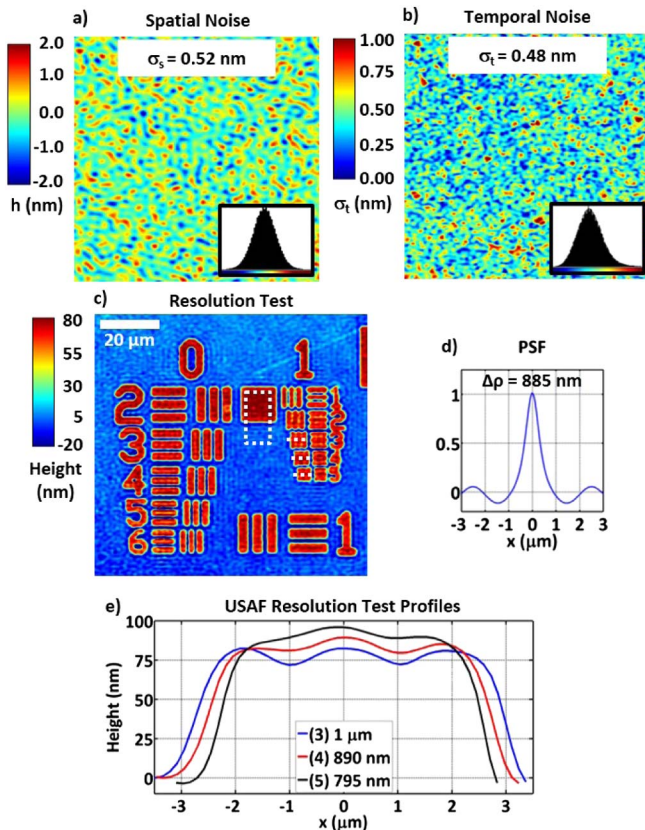
Fig. 3. High spatial coherence epi-wDPM system characterization. (a) Measured spatial noise. (b) Temporal noise. (c) epi-wDPM height map of USAF resolution target. The theoretical resolution is 875 nm. (d) Measured PSF obtained by measuring an edge (step response) and taking the derivative (impulse response). The resolution measured by the PSF is 885 nm. (e) Cross-sections taken from (c) showing the measured height profiles. The resolution measured from the cross-sections is 890 nm. Better resolution can be obtained by using a higher NA objective.

In order to characterize the noise of the epi-wDPM system, a flat, featureless portion of the sample was imaged. Ideally, the height should be zero everywhere, but small variations exist due to noise. Figure 3(a) shows the height map of a flat region where the standard deviation of the height in a given frame is used to quantify the spatial noise, which was measured to be 0.52 nm. Note that the surface roughness for quartz wafers coated with gold is about 0.34 nm [24]. To assess the temporal noise, a time sequence of 256 frames was acquired, and the standard deviation at each pixel over the sequence was computed as shown in Fig. 3(b). The measured temporal noise is 0.48 nm. Again, note that Fig. 3(a) shows height and Fig. 3(b) shows standard deviation. Figure 3(c) shows an epi-wDPM height map of the 1951 USAF resolution target. The point spread function (PSF) in Fig. 3(d) was obtained by measuring the edge (step response) indicated by the dotted rectangle, averaging along the horizontal dimension, and taking the derivative (impulse response) along the vertical. The distance from the peak to the first zero is a quantitative measure of the resolution under the Rayleigh criteria, resulting in a resolution of 885 nm. The theoretical resolution limit with a mean

wavelength of 574 nm, $NA_{obj} = 0.8$, and $NA_{con} = 0$ is 875 nm [11]. Figure 3(e) shows cross-sections from the 3, 4, and 5 series lines indicated by the dotted lines in 3(c). The respective line widths are 1 μm, 890 nm, and 795 nm. The 1-μm lines are resolved showing 3 distinctive peaks, the 890 nm lines are barely visible, and the 3 peaks cannot be identified in the 795-nm lines. Using the USAF resolution target, our measured resolution is about 890 nm, which agrees with the simple edge test from Fig. 3(d).

Figure 4 shows a comparison between white-light images with varying spatial coherence. We imaged HeLa cells cultured on a glass slide and coated with gold in a fashion similar to samples prepared for SEM [25]. Figure 4(a) shows an epi-wDPM (white light) image of a HeLa cell with the aperture diaphragm closed to its minimal value. Here, the intercellular structure is well defined indicating high contrast, but the measured heights are far below the correct values due to the lack of spatial coherence. Figure 4(b) shows the epi-wDPM image with proper spatial coherence, where the heights converge to their expected values, but the contrast is
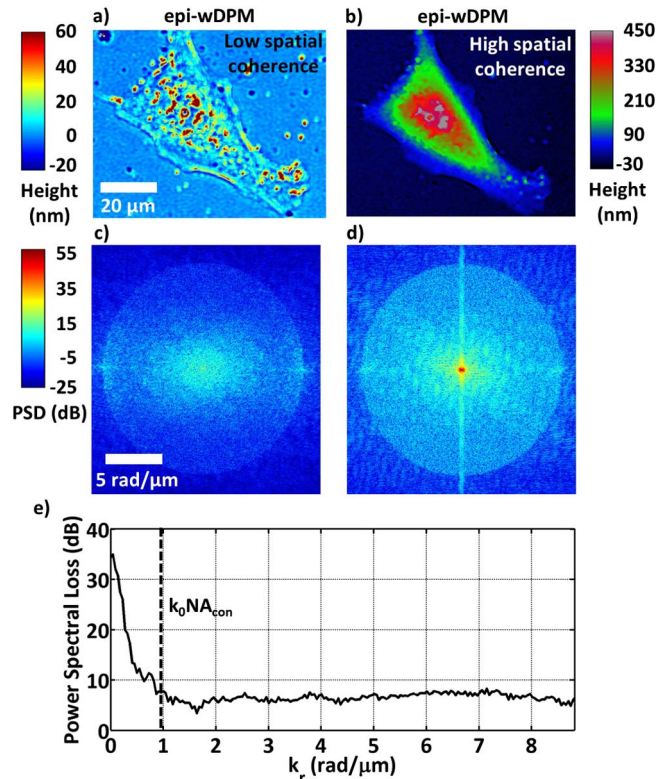

Fig. 4. Epi-wDPM with controllable spatial coherence. (a) White-light image with low spatial coherence showing intracellular details but incorrect height information. (b) White-light image with sufficient spatial coherence showing proper heights but less intracellular detail. (c), (d) Power spectra taken from the height maps in (a), (b). The vertical line in (d) is due to phase unwrapping. It is relatively weak and not visible on a linear scale. (e) Power spectral loss showing the difference between the azimuthally averaged coherent and incoherent spectra. The low spatial coherence case significantly attenuates the low-frequency content. The high spatial coherence case has a higher noise floor; this is reflected in the non-zero power spectral loss at high frequencies.

lower and the intercellular details are less apparent. The coherence area in epi-wDPM can be precisely controlled and tuned between the two extreme cases presented in Figs. 4(a) and 4(b) by using different pinhole sizes. When measuring structures where the height is important, high spatial coherence must be used, which means that much of the illumination is filtered out, and longer exposure times are required. When height is not important, but the details within a specimen are of more interest, low coherence imaging is preferred since it enables shorter exposure times and allows for faster dynamic measurements. The apparent added detail in the incoherent images is not due to better resolution, but rather the high–pass filtering effect resulting from the low spatial coherence. Figures 4(c) and 4(d) show the power spectrum taken from the height maps in (a) and (b) respectively. The visible outer circle is due to the cutoff from the finite numerical aperture of the objective. The circle has a radius of $k_0 NA_{obj}$. Figure 4(e) shows the power spectral loss, which is defined by first azimuthally averaging the coherent and incoherent PSDs individually using a linear scale, converting these averages to a logarithmic scale, and then subtracting the incoherent average from the coherent average. The low coherence approach has missing low frequency information, especially noticeable below $k_0 NA_{con}$, but it also has lower overall noise.

In summary, we presented the first reflection-based white-light DPM system. The results were verified by measuring control samples with known dimensions and comparing them to measurements from other well-established techniques. The system was characterized to show noise floors and resolution limits. We also imaged HeLa cells prepared for SEM imaging in order to show the trade-offs between low- and high-coherence wDPM. The integrated DPM system allows the user to easily select between the 4 imaging modalities: (1) DPM (laser transmission), (2) epi-DPM (laser reflection), (3) wDPM (white-light transmission), and (4) epi-wDPM (white-light reflection). This powerful new optical inspection tool can accommodate a wide variety of samples from various fields of study.

References

1. J. C. Wyant, Science **206**, 168 (1979).
2. D. J. Whitehouse, Meas. Sci. Technol. **8**, 955 (1997).
3. J. E. Castle and P. A. Zhdan, J. Phys. D **30**, 722 (1997).
4. J. H. Jang, W. Zhao, J. W. Bae, D. Selvanathan, S. L. Rommel, I. Adesida, A. Lepore, M. Kwakernaak, and J. H. Abeles, Appl. Phys. Lett. **83**, 4116 (2003).
5. L. Deck and P. Degroot, Appl. Opt. **33**, 7334 (1994).
6. J. C. Wyant, Appl. Opt. **52**, 1 (2013).
7. P. Ferraro, C. Del Core, L. Miccio, S. Grilli, S. De Nicola, A. Finizio, and G. Coppola, Opt. Lett. **32**, 2233 (2007).
8. G. Popescu, *Quantitative Phase Imaging of Cells and Tissues* (McGraw-Hill, 2011).
9. K. Lee, K. Kim, J. Jung, J. Heo, S. Cho, S. Lee, G. Chang, Y. Jo, H. Park, and Y. Park, Sensors-Basel **13**, 4170 (2013).
10. G. Popescu, T. Ikeda, R. R. Dasari, and M. S. Feld, Opt. Lett. **31**, 775 (2006).
11. B. Bhaduri, C. Edwards, H. Pham, R. Zhou, T. Nguyen, L. Goddard, and G. Popescu, Adv. Opt. Photon. **6**, 57 (2014).
12. T. Ikeda, G. Popescu, R. R. Dasari, and M. S. Feld, Opt. Lett. **30**, 1165 (2005).
13. G. Popescu, L. P. Deflores, J. C. Vaughan, K. Badizadegan, H. Iwai, R. R. Dasari, and M. S. Feld, Opt. Lett. **29**, 2503 (2004).
14. B. Bhaduri, H. Pham, M. Mir, and G. Popescu, Opt. Lett. **37**, 1094 (2012).
15. C. Edwards, A. Arbabi, G. Popescu, and L. L. Goddard, Light Sci. Appl. **1**, e30 (2012).
16. T. Slabý, P. Kolman, Z. k. Dostál, M. Antos, M. Losták, and R. Chmelík, Opt. Express **21**, 14747 (2013).
17. J. W. Goodman, *Laser Speckle and Related Phenomena* (Springer, 1975).
18. F. Zernike, Science **121**, 345 (1955).
19. T. Wilson and C. J. R. Sheppard, Optik **59**, 19 (1981).
20. Z. Wang, L. Millet, M. Mir, H. Ding, S. Unarunotai, J. Rogers, M. U. Gillette, and G. Popescu, Opt. Express **19**, 1016 (2011).
21. C. Edwards, B. Bhaduri, T. Nguyen, B. G. Griffin, H. Pham, T. Kim, G. Popescu, and L. L. Goddard, Opt. Express **22**, 5133 (2014).
22. T. Nguyen, C. Edwards, L. L. Goddard, and G. Popescu, Opt. Lett. **39**, 5511 (2014).
23. H. V. Pham, C. Edwards, L. L. Goddard, and G. Popescu, Appl. Opt. **52**, A97 (2013).
24. K. Okumura, E. Higurashi, T. Suga, and K. Hagiwara, *4th IEEE International Workshop on Low Temperature Bonding for 3D Integration (LTB-3D)* (IEEE, 2014), p. 26.
25. E. R. Fischer, B. T. Hansen, V. Nair, F. H. Hoyt, and D. W. Dorward, Current protocols in microbiology Chapter 2, Unit 2B 2 (2012).